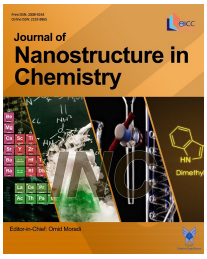

Volume 15, Issue 5, 152521 (1-16)

Journal of Nanostructure in Chemistry (JNSC)

https://doi.org/10.57647/jnsc.2025.1505.21

Dimensionality-Driven CQD/TiO_2-g-C_3N_4 Ternary Composites for Boosting Photocatalytic and PEC Performance

Tahira Bano[1], Shamaila Sajjad[1,*], Sajjad Ahmed Khan Leghari[2], Maria Murtaza[1], Rehana Riaz[1]

[1]*Faculty of Sciences, International Islamic University, H-10, Islamabad, 44000, Pakistan.*
[2]*Pakistan Institute of Engineering and Applied Sciences, Islamabad, Pakistan.*

[*]**Corresponding author:** shamaila.sajjad@iiu.edu.pk

Original Research

Received:
20 July 2025
Revised:
28 August 2025
Accepted:
5 October 2025
Published online:
20 October 2025

Abstract:

Photocatalysis and photoelectrochemical (PEC) water splitting are hindered by challenges such as rapid electron-hole recombination, limited visible light absorption, and inefficient charge transport. To overcome these limitations, a ternary composite CQD/TiO_2-g-C_3N_4 was engineered by combining 0D carbon quantum dots (CQDs), 1D TiO_2 nanorods, and 2D g-C_3N_4 nanosheets. This multidimensional structure significantly improves charge separation and transfer that enhances both photocatalytic and PEC efficiency. X-ray diffraction confirmed successful integration of TiO_2 and g-C_3N_4, with crystallite sizes ranging from 8.1 to 9.3 nm. SEM and TEM analyses showed uniform dispersion of TiO_2 nanorods on g-C_3N_4 sheets, while CQDs ($\sim 5-6$ nm) were attached to surface, establishing strong interfacial contact for efficient charge movement. UV-vis exhibited a redshift, indicating a narrower band gap, and PL analysis showed reduced electron-hole recombination. Under visible light, composite with 15.0 mL CQD displayed excellent photocatalytic activity, achieving 96.0% degradation of mixed dyes (MO + BPB) with clear linear degradation indicating consistant reaction rate and delivering a high PEC photocurrent density ($\sim$ 33 mA/cm^2). CQDs enhance charge separation and lower band gap while multidimension (0D–1D–2D) structure boosts charge transfer. The 0D–1D–2D architecture enhances charge mobility and light utilization, making this material highly effective for environmental cleanup and sustainable energy applications.

Keywords: Dimensionalities; Synergistic role; CQDs; Ternary composite; 2D g-C_3N_4

Cite this article: Bano, T., Sajjad, S., Khan Leghari, S.A., Murtaza, M., Riaz, R. Dimensionality-Driven CQD/TiO_2-g-C_3N_4 Ternary Composites for Boosting Photocatalytic and PEC Performance. *J Nanostruct Chem* **15**(5), 152521 (2025).

1. Introduction

The photocatalysis has emerged as a highly capable method to eliminate organic contaminants and split water to produce hydrogen in an eco-friendly and sustainable way [1, 2]. Effective photo catalysts should be cost effective, chemically stable and have high photocatalytic activity. N-type semiconductors such as TiO_2 and WO_3 etc are considered prototype photo-catalysts due to their exceptional chemical stability and conduction band edge at suitable potential level [3, 4]. Meanwhile, these materials practical applicability are limited since they absorb UV light in the complete solar spectrum and UV light increases efficiency of photo-generated exitons fast recombination.

Graphitic carbon nitride (g-C_3N_4) with low band gap was proposed as a next-generation photo-catalyst. g-C_3N_4 is a prominent organic polymeric semiconductor made entirely from non-metallic elements known for its non-toxic nature, strong chemical stability and effective utilization of visible light, due to its 2.7 eV band gap. Compared to other narrow band-gap semiconductor materials, it shows favorable valence and conduction band potentials of +1.6 eV/NHE and −1.1 eV, respectively [1]. These properties indicate that g-C_3N_4 is a highly effective, capable and functional for environmental cleaning and water splitting [5]. Despite its settlements, g-C_3N_4 has numerous limitations, like smaller precise surface area, fast charge carriers recombination rate, and the potential for H_2O_2 formation from opposing two-

electron reactions, which can disturb the photocatalytic efficiency for water splitting and hydrogen evolution [6]. Efforts to overcome these deficiencies have led to the development of effective methodologies, including g-C_3N_4 nanosheets, to increase the surface space [7]. Earlier studies have highlighted the benefits of heterojunctions in decreasing electron–hole recombination rates. For example, Wang et al. and Panimalar et al. established hydrogen production driven by visible light consuming MnO_2 and reforming carbon nanotubes with g-C_3N_4 composites [8, 9]. Similarly heterojunction of g-C_3N_4 with TiO_2 is extremely observed for attractive photocatalytic performance. Because TiO_2 band gap supports graphitic carbon nitride, allowing exchange of electrons from the conduction band of TiO_2 to g-C_3N_4, whereas VB of TiO_2 transports holes to g-C_3N_4 to drive redox reactions [10, 11]. To improve solar energy consumption, researchers have concentrated on improving its visible-light absorption through several approaches, such as structural amendment and morphological modification [12]. Therefore, adding TiO_2 with g-C_3N_4 to produce a porous nanocomposite with a large surface area is an inspiring strategy for improving photocatalytic performance [6]. TiO_2/g-C_3N_4 combinations with enhanced visible-light sensitivity have apprehensive escalating consideration in latest years [13, 14]. Several techniques have been discovered to achieve these improvements, such as stirring, bubbling, and the use of chemical agents, while fabrication of these heterostructures has been successfully employed through co-calcination and hydrothermal treatment method [15]. Besides, various heterojunction arrangements have been reported, including 0D/2D [6], 1D/2D [16], and core–shell structures [12]. These well-made heterojunctions may not only expand absorption of visible light but enhance the separation of photo induced exitons and downturn their recombination [7]. However, for TiO_2/g-C_3N_4 heterojunctions, interface electron–hole pairs traffic crowding has continued an in-expressive issue that blocks effective charge transport [8].

Additionally, the use of CQDs for their up-conversion fluorescence provides an opportunity to improve photo catalysis by expanding light absorption into ultraviolet or near-ultraviolet arrays. CQDs constitute a new group of carbon nanomaterials with outstanding qualities, including great bio-compatibility, size-dependent effects, strong solubility, transport abilities and effective electron acceptance. These prospects, linked with their cost-effectiveness, have led to their universal application in the photocatalyst strategy [17]. Owing to their nanoscale size, CQDs can generate close-fitting connections within photocatalysts, which support charge carrier recombination rates by enabling the transfer of photogenerated charges through various semiconductors [17, 18]. Earlier studies have confirmed that CQDs are capable of receiving electrons from other semiconductors and increasing light absorption. For example, CdS/CQD/g-C_3N_4 composites have greater degradation under visible, near-infrared (NIR) light when Z-structure charge transfer system is applied [19].

On the basis of a review of the present literature, we established a new graphitic carbon nitride nanocomposite (CQDs/TiO_2-g-C_3N_4) combination that is both light and cost-effective for photocatalysis. These composites were precisely constructed to increase the degradation of methyl orange [19, 20] and bromo-phenol blue as well as to expand the electrochemical (PEC) performance [21, 22]. The integration of 0D CQDs into the TiO_2/g-C_3N_4 medium strongly affects the water splitting reaction. CQDs improve the solidity at potentials and in electrolyte situations, which provides better PEC interpretation even at small applied potentials. This could be linked to a reduction in the number of effective sites offered for the PEC water splitting system [23]. In these composite assemblies, TiO_2 uses solar light efficiently due to its band gap i.e. 3.2 eV. The variation in g-C_3N_4 by the CQDs extends the absorption spectrum into the ultraviolet region ($\lambda < 380$ nm), potentially facilitating the induction of TiO_2 through photon-generated carriers [22, 24]. Our plan also integrates up-conversion fluorescence to spread visible light consumption, thereby facilitating successful chemical catalysis for the degradation of MO and BPB.

This research motivated the formation of unique multidimensional (0D/1D/2D) structure where 0D CQDs serve as rapid electron acceptors, 1D TiO_2 nanostructures act as charge transport pathways and 2D g-C_3N_4 sheets enable broader light absorption capabilities which creates a synergistic effect that maximizes interfacial charge separation and transfer. This hierarchical integration not only accelerates surface redox reactions but also broadens absorption range and minimizes charge recombination losses. Such cooperative interactions between multiple dimensionalities represent key innovation of this work and fundamental mechanism driving superior photocatalytic and PEC performance.

2. Experimental methods

2.1 2D graphitic carbon nitride (g-C_3N_4) fabrication

To synthesize graphitic carbon nitride nanosheets, combination of 6.0 g urea and thiourea in 1:1 ratio are used as precursors in a controlled thermal process. To prevent exposure to air, the crucible was tightly covered with Al foil. The crucible is then subjected to thermal treatment in a furnace, where it is heated to 400 °C for 1 h. This method ensures the production of nanosheets with the desired structural properties through a controlled chemical annealing process.

2.2 1D TiO_2 fabrication

To fabricate 1D TiO_2nanomaterials, 50 mL of NaOH solution and 5.0 mL of tetra butyl titanate (TBT) precursor were mixed. PH was carefully driven to 10 by gradually mixing with sodium hydro- oxide (NaOH) while stirring for 1.5 h. The combination was then treated hydrothermally in an autoclave at 160 °C for 4 h. Subsequently, the product was isolated by washing and centrifugation several times to remove impurities. After washing, the product was dried and calcined in an incinerator at 60 °C. Finally, calcined material was ground to produce a fine, white TiO_2 powder.

2.3 0D CQD fabrication

1.0 g of citric acid was melted in 40.0 mL of deionized water, stirred for 30 min to prepare the CQDs [25]. Citric acid was used as the carbon precursor in the hydrothermal synthesis of the CQDs. The subsequent solution was heated in hydrothermal instrument (oven) at 160 °C for 3 h. Compared to conventional high-temperature or vacuum-based techniques, the hydrothermal process uses a lot less energy and runs for a few hours at moderate temperatures ($160-200°C$) [22, 25]. The solution was examined in UV light, and a purple glow was observed. This indicates the successful formation of CQDs. This luminescence confirmed that the CQDs were ready for subsequent utilization.

2.4 Co-precipitation method for ternary composites

The fabrication of ternary composites, including g-C_3N_4, TiO_2, and CQDs, was achieved through a chemical method [26]. First, a binary nanocomposite of TiO_2 and g-C_3N_4 was fabricated by dissolving a specific amount of g-C_3N_4 with 2.0% TiO_2 in ethanol (40.0 mL). The mixture was sonicated for 40 min and then washed with ethanol for 30 min under centrifugation at 4000 rpm. The combination was subsequently dried at 70 °C for 3 h. The composite was subsequently partitioned into five equal parts. Four samples were combined with different proportions of CQDs (5.0, 10.0, 15.0, and 20.0 mL) and prepared (CQD/TiO_2-g-C_3N_4) ternary composites. These combinations were dehydrated by a hot plate, crushed into fine powders, and investigated for their photocatalytic activity. The fifth part is a binary composite for comparison with the ternary composites [25, 26]. The synthetic route of CQD/TiO_2-g-C_3N_4 nanocomposite is labelled in Scheme 1.

2.5 Photo catalysis experiment

The photocatalytic reactions of the fabricated composites were analyzed to degrade a mixed dye solution containing MO and BPB, each at a concentration of 10 mg, resulting in a total dye concentration of 20 mg/L. To determine the ideal dose, catalyst concentrations of 0.05 g are evaluated in 50 mL of dye solution [23, 26]. In a similar vein, various dye concentrations (10 mg/L, 20 mg/L, and 30 mg/L) were examined; These dye concentrations of 10 mg/L, 20 mg/L and 30 mg/L, have been widely reported in literature for photocatalytic degradation studies using g-C_3N_4 and composite-based photocatalysts [4, 12]. For each experiment, 0.05 g of the synthesized photo catalyst either TiO_2-g-C_3N_4 or CQD/TiO_2-g-C_3N_4 was added to 50 mL dye solution in a beaker. Photocatalytic degradation procedure was determined by initially keeping the solution in dark room for 30 min to simplify photocatalyst adsorption. After this adsorption period, samples (4.0 mL) were removed at 1h intervals under the radiation of a 1000 W xenon spotlight and immediately filtered to remove photocatalyst particles. It is significant to remember that the 1000 W xenon lamp applied in this research was only used as a laboratory light source to repeat ordinary lighting condition a controlled environment [4, 16]. Measured the absorption of the remaining contaminant and degradation percentage using UV–Vis Shimadzu 2700 spectrophotometer by detecting the absorbance peak specific to the dye which allowed the determination of variations in the absorbances of solutions corresponding to the concentrations of MO and BPB [18]. This process determines the photocatalytic ability over time. Every experiment was repeated three times, and deviation for each run was $\pm 3\%$.

2.6 Photoelectrochemical measurements

Photoelectrochemical experiments were performed using a work station (Correst potentiostat) with three-electrode classification, adjusting a standard calomel electrode (SCE), working electrode and a platinum counter electrode as a reference. The reversible hydrogen electrode (RHE) potential was measured via SCE analyses. To formulate the catalyst for the working electrode, 1.0 mg of the sample was liquefied in 10.0 mL of ethanol, subjected to ultrasonication for 1 h to attain a constant distribution, and then placed on fluorine-doped tin oxide (FTO) as a thin film substrate. Polarization bends were obtained via linear sweep

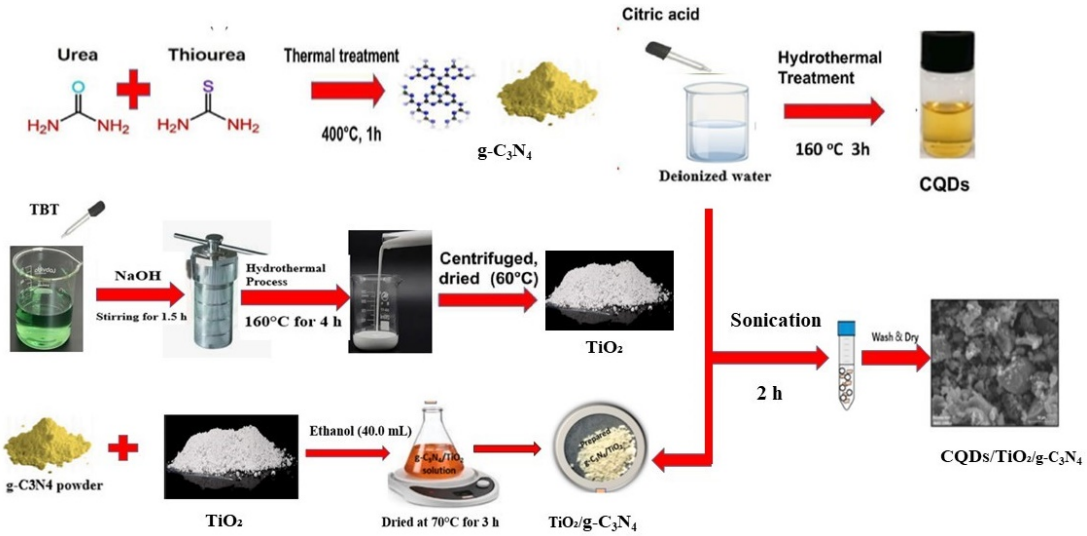

Scheme 1. Schematic diagram of CQD/TiO_2/g-C_3N_4 nanocomposite.

voltammetry (LSV) at 0.3 V versus NHE in a 0.5 M KOH electrolyte, which was sustained at a pH of approximately 12 and irradiated with $\lambda > 420$ nm. The photogenerated electrochemical cyclic voltammetry (CV) was implemented over five rounds at a scan rate of 20.0 mV/s. Furthermore, electrochemical impedance spectroscopy (EIS) was used to evaluate the system's proficiency under similar electrolyte and radiation atmospheres.

3. Characterization techniques

The sample morphology and composition were reviewed via SEM (JEOL-JAD 2300). Structural examination was conducted with X-ray diffraction using a Rigaku D/Max diffractometer with Cu Kα radiation (wavelength = 1.54 Å) functioned at 40 kV and 100 mA to determine the crystal structures. FT-IR spectra were recorded between 400 and 4500 cm^{-1} with a Model IR Tracer 100 spectrometer. UV–visible diffuse absorption and reflectance spectra were analyzed using a Shimadzu 2700 spectrophotometer. PL spectra were captured at ambient temperature with a Horiba Fluoromax-4 spectrofluorimeter. Raman spectra were obtained via a Horiba scientific Xplora spectrometer with a 532.0 nm YAG laser. PEC performance was assessed in a 3-electrode terminal cell with FTO glass coated with CQD/TiO_2-g-C_3N_4 composites using a standard calomel electrode (SCE) as the reference and a platinum counter as the working electrode, a saturated platinum electrode as the counter electrode, and 0.5 M KOH as the electrolyte. Photocurrent densities were measured at 100 mW/cm^2 from a 1000 W xenon arc lamp with an AM 1.5 G filter.

4. Results and discussion

4.1 Role of nanodimensionalities

The traditional systems usually include binary combinations such as CQDs/TiO_2 or TiO_2-g-C_3N_4, which often suffer from restricted charge separation and lacking light absorption. In difference, the CQD/TiO_2-g-C_3N_4 composite used a multidimensional structure combining 0D carbon quantum dots, 1D TiO_2nanorods, and 2D g-C_3N_4 nanosheets. This architecture strategy proposed several benefits such as, 2D g-C_3N_4 provides large surface area for catalytic reactions, improving the charge transfer efficiency. 0D CQDs act as electron mediators, trapping electrons and facilitating their transfer while also extending visible-light absorption through upconversion photoluminescence. This multidimensional synergy optimizes light harvesting, minimizes charge recombination, and significantly enhanced the photocurrent density ($\sim$ 33 mA/cm^2), than usually stated in the literature study. Therefore, this composite used as a photocatalyst not only surpasses old-fashioned TiO_2 structures in photocatalytic degradation but also indorse greater performance in photoelectrochemical water splitting.

4.2 X-ray diffraction (XRD) analysis

XRD was performed to calculate crystalline phases and structures of synthesized nanomaterials, as shown in figure 1 (A). The XRD results revealed distinctive peaks for g-C_3N_4, with prominent signals at 27.4° matching the (002) plane and a small intensity peak at 11.9° for the (100) plane. The result agrees well with prior findings by Wang et al., and Zhang et al. [27, 28]. This figure illustrates the materials interplanner stacking of the periodic tri-azine units and aromatic rings, respectively [29, 30]. The XRD graph of titania (anatase phase in Fig. 1 (A)) typically shows its most intense diffraction peak at $2\theta \approx 25.3°$, corresponding to the (101) plane, along with characteristic peaks at 37.8° (004), 48.0° (200), and 55.1° (211). These sharp peaks confirm the crystalline anatase structure of TiO_2. In the binary combination of TiO_2/g-C_3N_4 (Fig. 1 (A)) and CQD/TiO_2/g-C_3N_4 composites (Fig. 1 (B)), supplementary peaks for TiO_2 are detected at 27.4° (101), 33.3° (009), 37.5°, 40.8°, 45.5°, 53.4° (220), and 78.0° that endorse the effective combination of the components, as maintained in the literature using (PDF JCPDNo. 21–1272) [31], and other specific angles. However, their intensity decreases, possibly because of their low content or weak diffraction. In particular, the distinctive peak at 45.0° in CQD/TiO_2/g-C_3N_4 samples with 15.0 and 20.0 mL CQDSs is attributed to the high content of CQDs in composites specify a unique structural phase not generally detected in earlier studies. This is allocated to induced interface by the amplified CQD content. It distinguished them from other samples. The diffraction peaks of the CQDs in the other samples are not detected because of their low contents. For the (002) plane, the main peak intensity is slightly reduced. The XRD patterns also display a shift in the (100) peak of g-C_3N_4 to a small intensity compared with the intensified peaks at 64.0° and 78.2°, credited to the combination of TiO_2. The absence of CQD peaks in some samples suggests their low concentration. The Scherrer formula was used to determine the crystallite size of the composites which are given in Table 1.

4.3 Raman spectroscopy

Raman spectroscopy was used to measure the phase characteristics and structural changes in TiO_2/g-C_3N_4 binary and CQD/TiO_2-g-C_3N_4 ternary composites. A significant upfield shift in the vibration band occurred at the same point at 1044 cm^{-1} for both composites (Fig. 1 (C)) [32]. Similarly, peaks at 1276 and 1303 cm^{-1} were observed for both TiO_2/g-C_3N_4 and 15.0 mL-CQD/TiO_2-g-C_3N_4 composites. The shifts are linked to the interactions among the sigma bonds of g-C_3N_4 and oxygen vibrations of TiO_2 in composite [33]. Additionally, the TiO_2/g-C_3N_4 spectra exhibit prominent D and G band peaks at 1427 cm^{-1} and 1470 cm^{-1}, respectively, which signifies defects in the g-C_3N_4 carbon network [34]. The observed downfield shift in the ternary composite suggests the formation of new bonds or modifications in existing bonds, indicating that g-C_3N_4 may be integrated into the TiO_2 matrix rather than simply existing as a physical blend.

4.4 FTIR spectroscopy

FTIR spectroscopy, illustrated in figure 1 (D), was used to characterize functional groups present in the g-C_3N_4, TiO_2/g-C_3N_4 binary composite, and CQD/TiO_2-g-C_3N_4 ternary composites. FTIR investigation revealed the existence of g-C_3N_4, with characteristic peaks naturally observed in the $800 - 1900$ cm^{-1} range. The major peaks

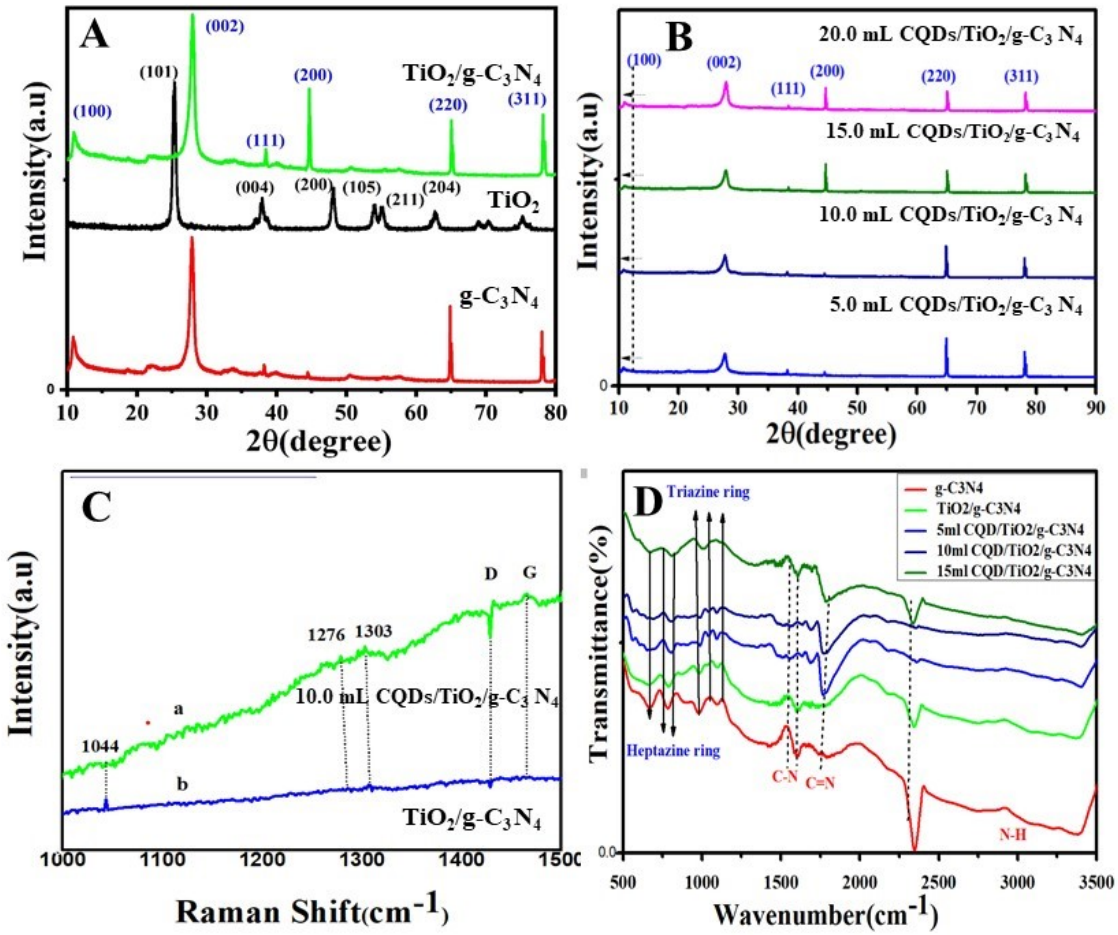

Figure 1. (A) XRD arrays of samples of 2D-g-C_3N_4, TiO_2 and TiO_2/g-C_3N_4 binary composites. (B) 5.0 mL-CQDs/TiO_2-g-C_3N_4, 10.0 mL CQDs/TiO_2-g-C_3N_4, 15.0 mL-CQDs/TiO_2-g-C_3N_4 and 20.0 mL-CQDs/TiO_2-g-C_3N_4. (C) Raman analyses of samples of the TiO_2/g-C_3N_4 binary composite and 15.0 mL-CQD/TiO_2/g-C_3N_4 ternary composite. (D) FT-IR spectra of various pure and binary and ternary composites.

at $500-700$ cm^{-1} were observed for Ti-O and Ti-O-Ti stretching modes [35]. Remarkably, spectra show distinctive vibrational modes connected with g-C_3N_4, containing the heptazine ring breathing mode at approximately 750-808 cm^{-1} and additional peaks between 809 and 1200 cm^{-1}. These results are in consistent with the triazine group's vibrations as reported in earlier research studies [36]. Extending vibrations were apparent between 1200 and 1650 cm^{-1}, with definite peaks at 1540 cm^{-1} and 1650 cm^{-1} related to C–N and C=N bond broadening, respectively with previous documented [35, 37].

The peak at 2363 cm^{-1} was attributed to CO_2 molecules on the surface. N-H broadening was detected between 2830 and 3500 cm^{-1}, associated with NH_2 or NH groups at defective sites in aromatic ring [38]. These explanations support presence of g-C_3N_4 in samples. However, the FTIR data alone do not elucidate whether g-C_3N_4 is simply mixed with TiO_2 or has been integrated into the TiO_2 lattice.

4.5 Optical studies

To evaluate the light absorption efficiency, diffuse reflectance spectroscopy was utilized, and results are shown in figure 2 (A). TiO_2 exhibited light absorption primarily below 375 nm, which is consistent with earlier research [39]. In contrast, the incorporation of g-C_3N_4 into TiO_2 extended absorption wavelength to 470 nm. This finding indicates

Table 1. Crystalline sizes and bandgaps of the pure, binary and ternary composites.

Composites	Crystallite Size (nm)	Bandgap (hc/λ) eV
g-C_3N_4	9.0	2.75
TiO_2/g-C_3N_4	8.1	2.63
5.0 mL CQDs-TiO_2/g-C_3N_4	8.8	2.59
10.0 mL CQDs-TiO_2/g-C_3N_4	8.6	2.43
15.0 mL CQDs-TiO_2/g-C_3N_4	8.7	2.27
20.0 mL CQDs-TiO_2/g-C_3N_4	9.3	2.33

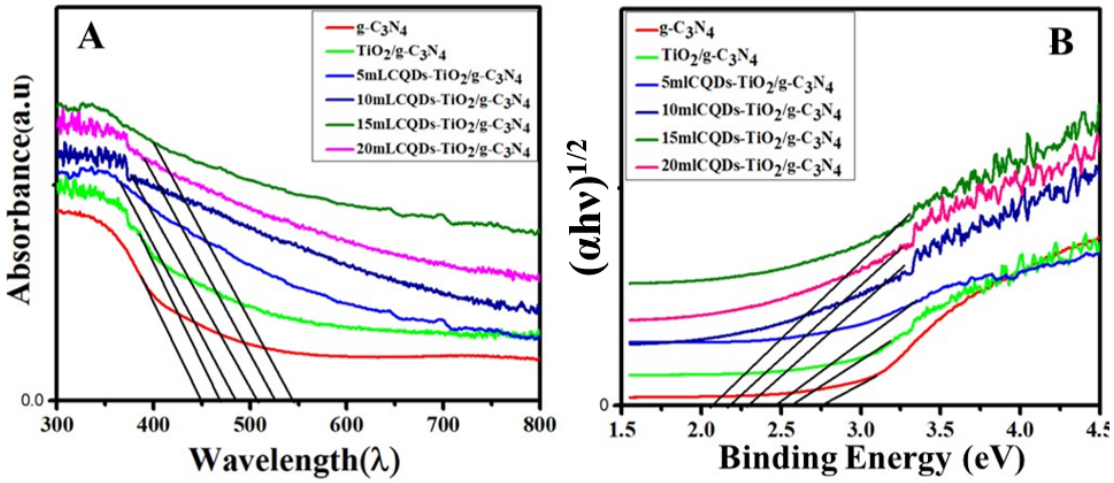

Figure 2. (A) UV–visible DRS absorbance spectra, (B) corresponding bandgap photon energy values of 2D-g-C_3N_4 and TiO_2/g-C_3N_4 binary composites, 5.0 mL-CQDs/TiO_2-g-C_3N_4, 10.0 mL CQDs/TiO_2-g-C_3N_4, 15.0 mL-CQDs/TiO_2-g-C_3N_4 and 20.0 mL-CQDs/TiO_2-g-C_3N_4 ternary composites.

that heterojunction between two materials enhances light absorption. Furthermore, the addition of CQDs to TiO_2/g-C_3N_4 led to an increased absorption edge that extended into the infrared region [40]. This redshift in the absorption spectrum suggests a reduction in the photocatalyst bandgap, as shown in Fig. 2 (B). This is linked to redox potential of the photogenerated charge carriers. CQDs act as electron acceptors and do not influence the VB directly. They contribute to a broader conduction band (CB) by shrinking the band gap [41]. This adjustment reduces the electron capacity for reduction in the conduction band but is offset by enhanced visible light absorption which is agreed with pervious report of Y. Deng et al. that CQDs showed up-conversion materials absorbing visible light, which initiates TiO_2 to produce electron–hole pairs [40]. This mechanism improves degradation efficiency of pollutants under both UV and visible light irradiation. Consequently, a redshift of the absorption edge within a specific range can improve photocatalytic performance by increasing efficiency of light utilization and enhancing overall photocatalytic activity.
The photocatalytic efficiency decreased when the redshift effect could not be effectively counterbalanced by increased light absorption [42]. The optimal photocatalytic activity for TiO_2/g-C_3N_4 composites altered with CQDs was observed at 15.0 mL and 20.0 mL, where the enhanced visible light absorption sufficiently mitigated the redshift effect. However, at CQD loadings exceeding 15.0 mL, the redshift effect offset the benefits of increased visible light absorption, leading to reduced catalytic performance. Bandgap analysis via the Tauc plot method in Fig. 2 (B) indicated that g-C_3N_4, TiO_2/g-C_3N_4 and CQDs-TiO_2-g-C_3N_4 (5.0, 10.0, 15.0 and 20.0 mL concentrations of CQDs, respectively) have bandgaps of approximately 2.7, 2.6, 2.5, 2.4, 2.2 and 2.3 eV, respectively (Fig. 2 (B) and Table 1).

4.6 PL spectroscopy analysis

Photoluminescence (PL) spectra are dynamic for evaluating charge separation, recombination dynamics, and radiation mechanisms in photocatalysts, as displayed in Fig. 3. The PL spectra of g-C_3N_4 show two distinctive radiation peaks at 439 nm and 479 nm, which are linked with sp^3 C–N (σ) and sp^2 C–N (π) bond transitions, respectively which show similarity with the result reported earlier [43]. Upon the addition of TiO_2 and the CQDs, the PL intensity clearly decreases, with slight peak shifts. Certainly, integrating CQDs into TiO_2/g-C_3N_4 nanocomposites leads to strong PL quenching, which is generally visible in 15.0 mL of TiO_2/g-C_3N_4 composite. This outcome is attributed to intensified p-p interfaces and the creation of a type II van der Waals heterojunction, which efficiently decreases charge carrier recombination [44]. Moreover, a bathochromic shift in the PL spectra results in the highest radiation peak changing from 429 to 432 nm and 479 to 474 nm in the 5.0 mL-CQDsTiO_2/g-C_3N_4 sample, which is likely an overview of the subgap defects incorporated by the nanomaterials [44, 45].

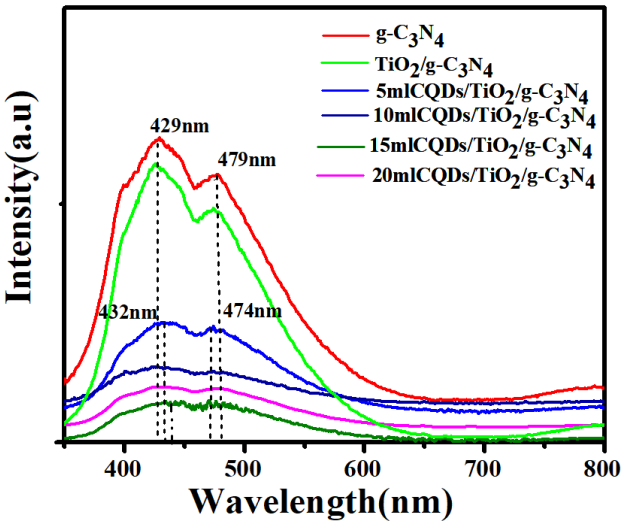

Figure 3. Photoluminescence composite spectra of 2D-g-C_3N_4 and TiO_2/g-C_3N_4 binary composites, 5.0 mL-CQDs/TiO_2-g-C_3N_4, 10.0 mL CQDs/TiO_2-g-C_3N_4, 15.0 mL-CQDs/TiO_2-g-C_3N_4 and 20.0 mL-CQDs/TiO_2-g-C_3N_4 ternary composite spectra at an excitation wavelength of 330 nm at standard temperature.

4.7 Morphology and composition analyses

Scanning electron microscopy and energy dispersive X-ray spectroscopy were used to analyze morphology and composition of samples. Figure 4 shows SEM images and EDX results for pure g-C_3N_4, revealing a non-uniform 2D nanosheet structure at scales of 1 µm and 500 nm. SEM images revealed the 2D sheet morphology of g-C_3N_4, which is crucial for optimizing its properties in composite formation. Figure 4 shows SEM images of the TiO_2/g-C_3N_4 composite, highlighting the integration of 1D TiO_2 rods within the 2D g-C_3N_4 sheets. The addition of 0D CQDs in TiO_2/g-C_3N_4 composite, as shown in Fig. 4, led to significant morphological changes, with a prominent stacked sheet-like structure visible in the 15.0 mL CQD/TiO_2/g-C_3N_4 composite. The CQDs, which are difficult to detect because of their smaller size, are dispersed on the surface of TiO_2/g-C_3N_4 sheet, as shown by black dots.

EDX spectroscopy was applied to examine the elemental arrangement of generated samples, as shown in Fig. 4. The EDX spectrum of 2D g-C_3N_4 nanosheets revealed the presence of carbon (C) and nitrogen (N) peaks, indicating the effective generation of g-C_3N_4 with no evident impurities. For the TiO_2/g-C_3N_4 binary composite and the 15.0 mL-CQD/TiO_2-g-C_3N_4 ternary composition (Fig. 4), supplementary peaks for titanium (Ti) and oxygen (O) are detected. The EDX spectrum of ternary composite contains signals for C, N, O and Ti, confirming the integration of CQDs and TiO_2. The differences in the spectra, particularly the existence of CQDs and TiO_2 peaks, confirm effective incorporation of these components. Table 2 presents the qualified elemental conformations of created samples.

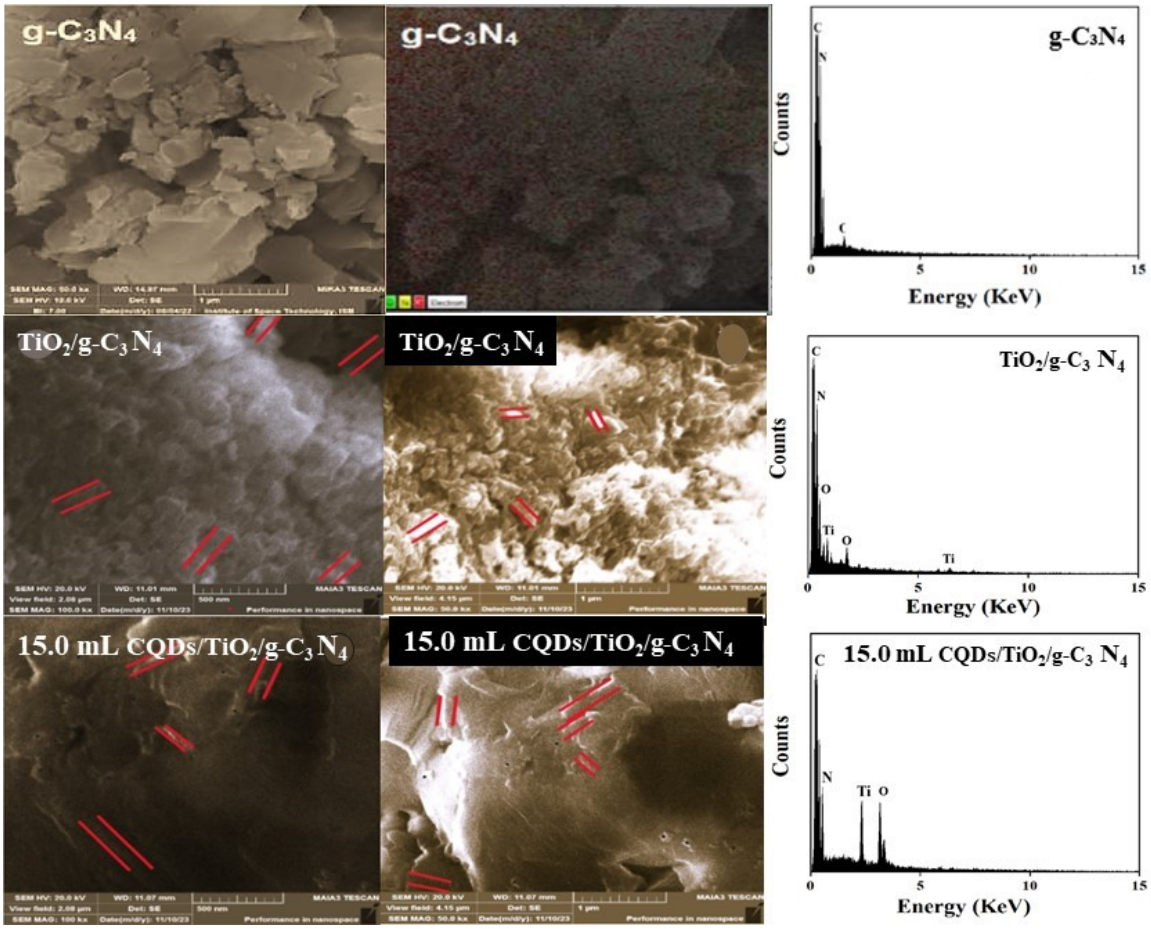

Figure 4. SEM images and EDS results of the prepared samples of the g-C_3N_4, TiO_2-g-C_3N_4 binary composite and 15.0 mL-CQD/TiO_2/g-C_3N_4 ternary composite at different magnifications.

Table 2. Elemental composition of synthesized samples.

Composites	TiO_2/g-C_3N_4		15.0 mL CQDs/TiO_2-g-C_3N_4	
Element	Weight %	Atomic %	Weight %	Atomic %
C	31.13	35.89	30.46	37.56
N	44.38	43.88	36.91	39.02
O	18.42	15.95	22.90	21.20
Ti	0.08	0.02	0.24	0.07

4.8 TEM analysis

The TEM images in Fig. 5 show the structure and morphology of the 15.0 mL-CQD/TiO_2-g-C_3N_4 heterojunction. The 2D g-C_3N_4 stacked nanosheets are shown in Fig. 5 (a,b). These regions appear as thin, sheet-like, or layered regions with extended planar dimensions. The faint, transparent, and slightly overlapping regions indicate the presence of 2D nanosheets or layered structures. On large scale lamellar structured aggregation is detected which is in agreement with the result [46]. There are dark regions and gray areas exist. The dark portion of the rod forms TiO_2, whereas the light gray area is allocated to the 2D g-C_3N_4 stacked sheet, confirming that the 1D TiO_2 are wrapped inside the g-C_3N_4 sheets. Moreover, TiO_2 is well dispersed on 2D g-C_3N_4 nanosheets, indicating that the presence of g-C_3N_4 suppressed the aggregation of TiO_2 [46]. In addition, the TiO_2 nanowires in the g-C_3N_4 sheet, which are openly dissimilar from TiO_2, indicate that the composites were effectively formed [31]. The CQDs that appear as small, bright, and well-defined nanoparticles are circled in the image to analyze the size distribution of the CQDs on the samples. According to the elemental mapping analysis, C, N, O and Ti were present in the 15.0 mL-CQD/TiO_2/g-C_3N_4 composite.

5. Photocatalytic activity

The photocatalytic degradation was determined by using the pure g-C_3N_4, binary and ternary photocatalysts under visible light. The catalysts consisted of 2D g-C_3N_4 nanosheets with TiO_2 and further altered with varying quatities of quantum dots (CQDs) (5.0, 10.0, 15.0 and 20.0 mL). To confirm the highest absorption, each sample was originally placed in a dark chamber for 30 min before subjected to light intensity. The degradation efficiency of the photocatalysts was determined by the absorbance of the MO & BPB dyes. The results shown in Fig. 6 (A) reveal outstanding differences in the degradation of MO & BPB over different samples. In particular, the composites TiO_2-g-C_3N_4, and with 5.0, 10.0, 15.0, and 20.0 mL of CQDs displayed degradation profiles of 45.2, 67.5, 79.0, 96.0, and 82.0%, respectively. The composite with 15.0 mL of CQDs/TiO_2-g-C_3N_4 had the highest photocatalytic activity, resulting in maximum absorption and an excellent degradation ratio of 96.0%, as shown in Fig. 6 (B). Moreover, the maximum ratio of the ternary composites with 15.0 and 20.0 mL-CQDs was verified for the degradation of both MO and BPB, indicating their higher photocatalytic efficiency. Figure 6 (C) presents the degradation kinetic constant for all the samples. The 15.0 mL CQD/TiO_2-g-C_3N_4 composite displayed higher photocatalytic performance with the highest degradation kinetics. This investigation highlights the role of TiO_2 and CQDs in increasing photocatalytic proficiency through the optimization of electron–hole pair recombination rates and improved flourescence responces. This observed performance supports well with the work reported that the composites of TiO_2/g-C_3N_4 heterojunction structures for active degradation of dyes [47]. The g-C_3N_4 serves as the foundational photocatalyst in photocatalytic activity, primarily due to its suitable medium bandgap (2.7 eV), which enables strong visible-light absorption, and excellent chemical stability, thus making it an effective material for heterojunction

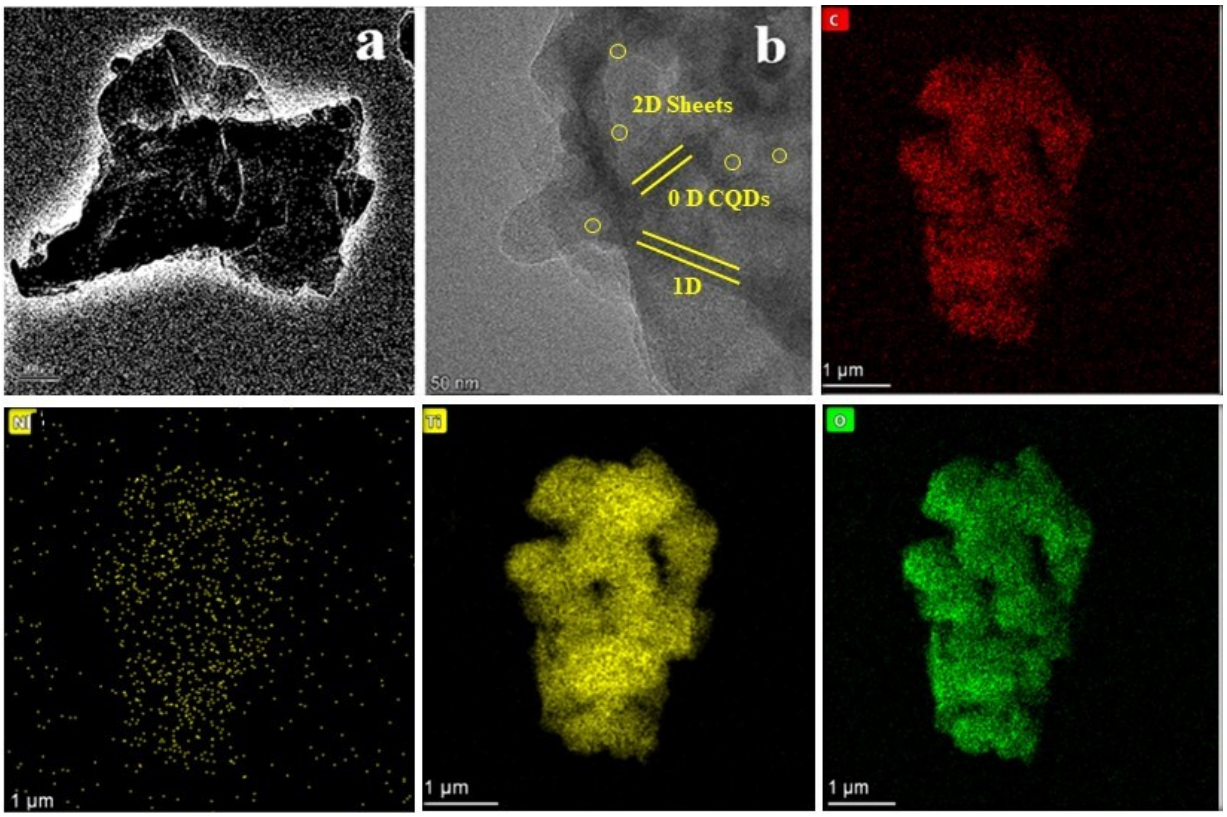

Figure 5. TEM image of 15.0 mL CQD/TiO_2-C_3N_4 heterojunctions at different nanoscales (a, b) and elemental mapping of 15.0 mL CQD/TiO_2-g-C_3N_4 ternary composites.

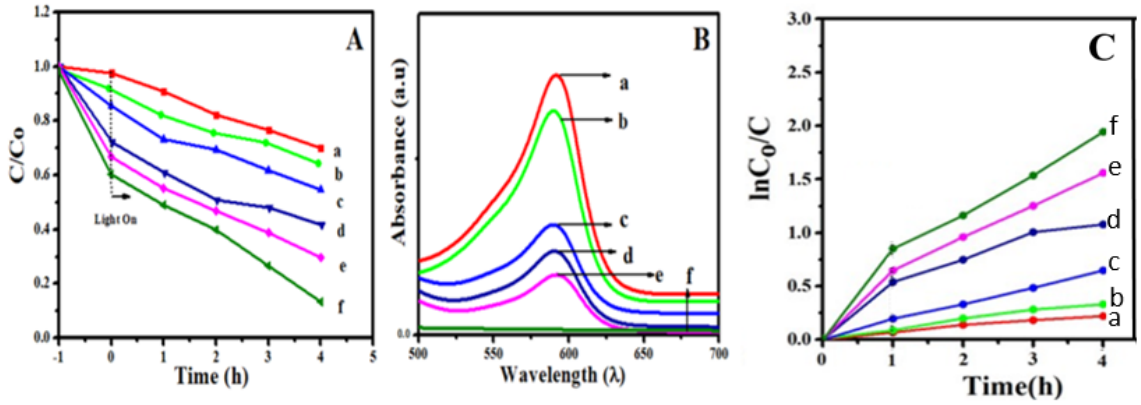

Figure 6. (A) Effect of the reactive photocatalyst on the simultaneous degradation of MO & BPB and time-dependent solar-driven catalytic degradation over (a) g-C_3N_4,(b) TiO_2/g-C_3N_4,(c) 5.0 mL of CQDs-TiO_2/g-C_3N_4,(d) 10.0 mL of CQDs-TiO_2-g-C_3N_4,(e) 20.0 mL of CQDs-TiO_2-g-C_3N_4 and (f) 15.0 mL of CQDs-TiO_2-g-C_3N_4, (B) UV visible absorption spectra of 15.0 mL of CQDs-TiO_2-g-C_3N_4 showing the highest degradation after five hours of the reaction process, and (C) kinetic study of synthesized samples for the degradation of dyes for 4 hours.

formation with TiO_2 and CQDs. Its 2D layered structure provide a vast surface area and active spots, whereas its nitrogen rich structure enables strong interaction with contamination. When g-C_3N_4 integrated with TiO_2, forms a heterojunction that magnifies charge separation by stimulating the migration of photo induced charges-carriers in opposite direction, therefore reducing charge recombination [41, 47]. In combination CQDs supports the photocatalytic system by acting as electron mediators and contributing up-conversion photoluminescence, which permits the utilization of low energy photons that would otherwise be lost [40]. This amazing co-operation among g-C_3N_4, TiO_2, and CQDs significant to effective charge transfer, sustained light absorption, and the generation of reactive oxygen species (ROS), remarkably enhance the degradation of contaminants or hydrogen production under visible light [48]. Generally, graphitic carbon nitride (g-C_3N_4) works as an active visible light sensitizer and structural effective in CQDs/TiO_2-g-C_3N_4 nanocomposites, making it significant component for photocatalytic efficiency booster. To increase the photocatalytic efficiency, quantum dots (CQDs) were integrated into TiO_2/g-C_3N_4 heterojunctions with quantities of 15.0 and 20.0 mL. This formation was deliberate to increase electron transmission inside the photocatalytic system [49]. The CQDs significantly increased the photocatalytic activity by increasing electron transfer and decreasing electron-hole recombination. These result are agreed well with the mechanisim and performance enhancement reported in their study [50]. The addition of CQDs at specific concentrations thus proved essential for achieving the highest levels of photocatalytic activity, as shown in Fig. 6 (C). The photocatalytic degradation of MO and BPB followed pseudofirst kinetics, as clearly described by the following equation:

$$\ln\left(\frac{C_0}{C}\right) = \text{kapp} \times t \quad (1)$$

where C_0 denotes the primary concentration before radiation at $t = 0$, C is the concentration after radiation t represents the time in solution, and kapp signifies the apparent degradation rate.

A reliable study revealed that the existence of TiO_2 improved the automatic properties of g-C_3N_4, thereby improving its photocatalytic performance [46]. Additionally, the combination of CQDs further increased this movement, with the 15.0 mL CQD composite displaying the best performance in environmental remediation applications over effective dye degradation [51, 63, 64]. The degradation proficiency of g-C_3N_4 composites was promisingly enhanced with the integration of CQDs, increasing from 28.0% to 96.0% as the CQD loading increased. When 15.0 mL of 0D-CQDs were integrated, the degradation ratio reached 96.0%. This degradation ratio subsequently decreased to 82% at a loading of 20.0 mL of CQDs. The maximum degradation efficiency of 96.0% was observed with 15.0 mL of CQDs added to the TiO_2/g-C_3N_4 composite, as represented in Fig. 6 (C).

The synthesized photocatalyst was used in this study to investigate various concentrations of MO & BPB pollutants (10, 20, and 30 ppm), as illustrated in Fig. 7 (A). The best concentration for assessing photocatalytic performance was found to be 20 ppm solutions of both MO & BPB, which demonstrated the maximum degradation efficiency among them. The best photocatalyst in this research study, 15.0 mL CQDs/TiO_2/g-C_3N_4, was tested in triplicate to evaluate its stability and reproducibility. Figure 7 (B) illustrates the graph depicting the photocatalyst's consistent performance over repeated cycles. The catalyst retained the photoactivity of 83% after three cycles of reusability. Table 3 presents the comparison of the performance of various TiO_2/g-C_3N_4-based nanocomposite for the photocatalytic degradation of different dyes and pollutants.

6. Catalytic mechanism

The photocatalytic performance of CQDs/TiO_2-g-C_3N_4 of degradation of methyl orange (MO) and bromophenol blue (BPB) under visible light is governed by synergistic interacting among the 0D, 1D, and 2D components, which facilities superior light harvesting, charge carrier sepration, and reactive oxygen species (ROS) generation. UV–vis diffuse reflectance spectroscopy (DRS) measurements confirm TiO_2 and g-C_3N_4 band gaps of approximately 3.38 and 2.72 eV, respectively [59]. Based on the empirical equations for

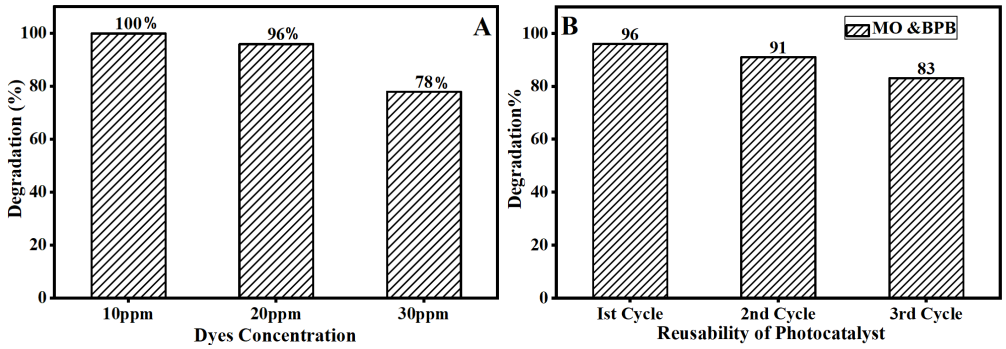

Figure 7. (A) Photocatalytic degradation of Dyes (MO & BPB) with changed dye concentration, (B) Reusability experiments of the most effective photocatalyst 15.0 mL CQDs/TiO_2/g-C_3N_4, over three cycles.

band edges position [65], TiO_2 possesses conduction band (CB) and valance band (VB) potentials of −0.43 and +3.05 eV, while g-C_3N_4 exhibits CB and VB positions at −1.44 eV and +1.88 eV, respectively. These band alignments from a type II hetrojunction structure, where the CB electrons from g-C_3N_4 are energetically favorable to migrate to TiO_2, and the VB holes from TiO_2 shifts to g-C_3N_4. This spatial charge sepration significantly reduces recombination rate of photogenerated electron hole pairs, which is one of major challenges in photocatalysis (Low J, et al.) [66]. The CB potential of TiO_2 is greater than that of g-C_3N_4, and negative ion (electron) transfer occurs from g-C_3N_4 to TiO_2. Conversely, holes transfer from TiO_2 to g-C_3N_4 due to the smaller VB potential of g-C_3N_4 than that of TiO_2. This effective transmission of photoinduced charge carriers decreases the recombination rate, thereby improving the photocatalytic activity. The inclusion of zero-dimensional (0D) CQDs further enhance the system by acting as efficient electrons mediators and photosensitizers. Their unique upconversion photoluminescence (UCPL) from properties allow them to absorb long- wavelength visible light and emits shorter wavelength, thereby facilitating light absorption and efficiently transfer them to one-dimensional (1D) TiO_2, refining the charge mover confinement at the TiO_2/g-C_3N_4 edge [67]. Moreever, CQDs introduces abundant π− conjugated surface and surface functional groups that facilitate rapid electron transfer. Electrons can be captured from g-C_3N_4 by CQDs and then shuttled to TiO_2, minimizing recombination losses and promoting continuous redox rection [14]. Upon visible light irradiation, both CQD and g-C_3N_4 are excited, the CQD/TiO_2-g-C_3N_4 composite producing electrons in the CB and holes in the VB. These charge carriers react with absorbed water (H_2O) and molecular oxygen (O_2) to form hydroxyl radicals ($^{\bullet}OH$) and superoxide radicals ($^{\bullet}O_2^-$), which are the primary active species in the dye degradation. The VB potential of TiO_2 (+3.05 eV) is more positive than the oxidation potential of $H_2O/^{\bullet}OH$ (2.68 eV), enabling the generation of $^{\bullet}OH$ radicals through hole oxidation [68]. Meanwhile, the CB of g-C_3N_4 (−1.44 eV) is more negative than the reduction potential of $O_2/^{\bullet}O_2^-$

Table 3. Comparison of the performance of various TiO_2/g-C_3N_4-based nanocomposite for the photocatalytic degradation of different dyes and pollutants.

Photo catalyst	Pollutants	Initial concentration	Light source	Time (min)	Degradation (%)	References
g-C_3N_4/CQDs	Rh B	10.0 mg/L	300 W Xe lamp	60	90.9	[51]
Ag/g-C_3N_4	AV-7 dye	20.0 mg/L	100 W Xe lamp	100	48	[52]
g-C_3N_4/TiO_2	MO	10.0 mg/L	300 W Xe lamp	300	40.0	[53]
C-TiO_2/g-C_3N_4	MO	10 mg/L	300 W Xe lamp	60	99.0	[54]
g-C_3N_4-TiO_2-GA	RhB	20.0 mg/L	500 W Xe lamp	60	98.0	[55]
TiO_2/rGO/g-C_3N_4	RTB	10.0 mg/L	500 W Xe lamp	90	60.0	[56]
CdS/CQDs/g-C_3N_4	RhBM	10.0 mg/L	300 W Xe Lamp	20	100.0	[57]
TiO_2/g-C_3N_4/RGO	RhB	10.0 mg/L	500 W Xe lamp	60	99.0	[58]
g-C_3N_4/TiO_2 NTs	RhB	5.0 mg/L	300 W Xe lamp	150	99.0	[59]
TiO_2/C_3N_4	Congo Red	10.0 mg/L	300 W Xe lamp	60	91.0	[35]
g-C_3N_4/TiO_2 NTs	SMT	5.0 mg/L	450 W Xe lamp	300	100.0	[60]
g-C_3N_4-TiO_2	MB	10.0 mg/L	300 W Xe lamp	180	80.0	[61]
TiO_2/C/g-C_3N_4	MO	0.2 mol/L	Sunlight irradiation	180	93.6	[62]
CQDs/TiO_2/g-C_3N_4	MO & BPB	20.0 mg/L	1000 W Xe lamp (Visible Light Source)	300	96.0	Present Work

(−0.33 eV), favoring superoxide radical formation via electron reduction [51, 69]. This charge transfer route involving CQDs helps maintain strong redox ability on both the TiO_2 and g-C_3N_4 sides, unlike simple type-II systems that often suffer from reduced oxidative/reductive potentials. CQDs also serves to trap and gradually release charge carriers, extending their liftimes and increasing the reaction window for ROS generation. This mechanism explains the role of $^{\bullet}OH$ radicals in the effective degradation of MO and BPB as shown in Fig. 8.

7. Useful application of degradation in different water sourses

The influence of various water sources on the photocatalytic degradation of methyl orange (MO) and bromophenol blue (BPB) by applying prepared photocatalysts in the ternary composite 15.0 mL-CQDs/TiO_2-g-C_3N_4 was investigated to understand their practical application for the purification of water. Water quality significantly affects photocatalytic efficiency. As depicted in Fig. 9 (A), the degradation ratios achieved with different water types were as follows: Drain water exhibited a 20.0% degradation rate, stream water 32.2%, river water 40.0%, tap water 49.0%, and underground water 80.3%. The associated degradation kinetic constants were 0.01057, 0.01696, 0.02268, 0.04163, and 0.05195 min^{-1}, respectively, as shown in Fig. 9 (B) for practical application. Water quality is the most important factor; therefore, different backgrounds of water were used and investigated for degradation of environmental pollutants (MO & BPB) by using the synthesized photocatalyst, which has the best performance in terms of catalytic activity in this study. The greatest inhibition effect on degradation occurred in the drain water, followed by the stream water, which revealed that several other pollutants exist, such as organic matter or anion inhibitors. Therefore, in this study, the degradation ratios decreased due to the addition of other organic or inorganic anions, as we revealed that underground water and tap water produced more pollutants than drain and stream water did. Thus, the maximum degradation is occurred for MO and BPB in terms of their photocatalytic activities in underground water and tap water. The reduced degradation process in certain water sources may be attributed to the presence of anionic inhibitors and/or competing organic substances, which likely interfere with the efficiency of the photocatalytic process.

8. Photo electrochemical activity

Due to quantum confinement, a reduced recombination rate of photogenerated electron–hole pairs enhances the reduction properties of samples according to their PL characteristics [45]. Photo-generated H_2 gas was evaluated by the use of CQDs/TiO_2-g-C_3N_4 under visible light. In OER, g-C_3N_4 and TiO_2/g-C_3N_4 display very poor performance, which might be due to the collection of H_2O_2, which devalues plain catalysts and decreases the current concentration. A very minor improvement in the current concentration was detected for the CQDs/TiO_2-g-C_3N_4 (20.0 mL). The CQD/TiO_2-g-C_3N_4 (15.0 mL) composites were exposed to the excessive current. Similarly, photoinduced holes on the surface of g-C_3N_4 oxidize water to produce O_2 and H_2O_2. CQDs offer a supplementary path and overturn rate of H_2O_2 molecules [70]. It is apparent from the spectra that the CQD/TiO_2/g-C_3N_4 (15.0 mL) composite has a more powerful photocurrent density than all the other composite materials. This highlights the new fabrication of photoinduced electrons and the greater departure rate of photoinduced electron–hole pairs, which was also realized in the PL investigation. This characteristic accounts for the enhanced performance of the samples in the photoelectrochemical and photocatalytic degradation of organic contaminants.
LSV was used for the analysis of the HER of the samples in a 0.5 M KOH electrolyte. Figure 10 (A) depicts the HER polarization curves (current densities vs. reversible hydro-

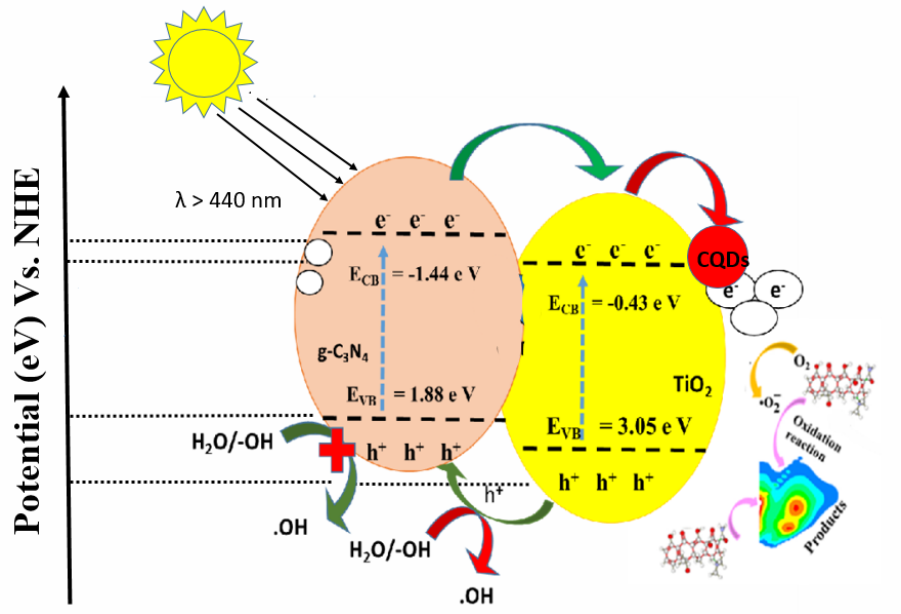

Figure 8. Hypothesized pathways for the photocatalytic degradation of MO & BPB on CQDs/TiO_2-g-C_3N_4 when exposed to visible light.

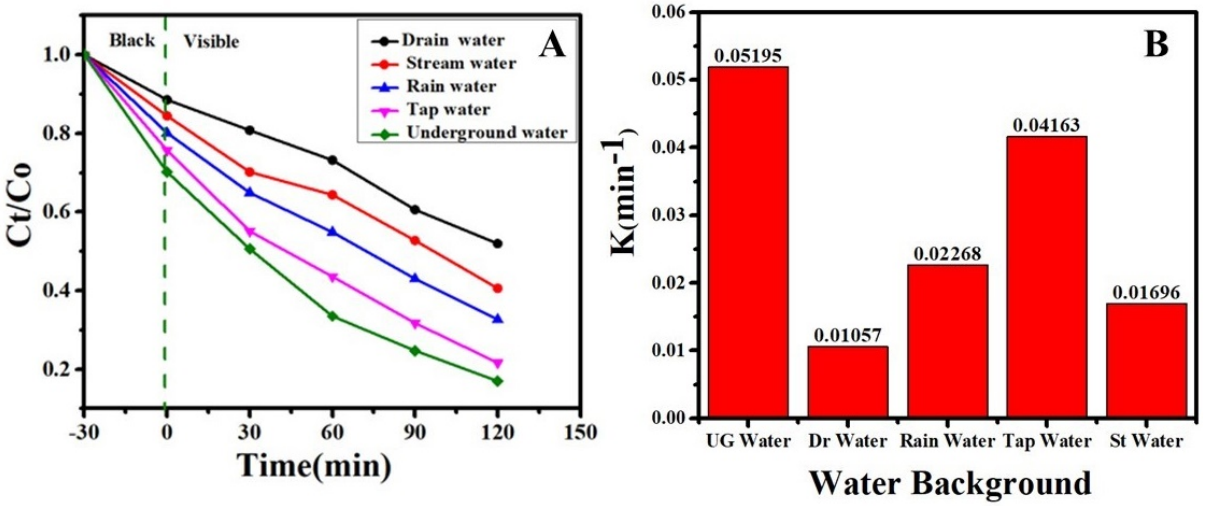

Figure 9. (A) The effect rates of different water background sources on water pollution (MO and BPB) breakdown by CQDs/TiO_2-g-C_3N_4 from different water sources. (B) shows the differences in the degradation kinetic constants for each water source.

gen electrode (RHE)) of electrodes based on TiO_2/g-C_3N_4 and TiO_2/g-C_3N_4 with concentrations of 10.0, 15.0 and 20.0 mL of CQDs, respectively. The results revealed that TiO_2/g-C_3N_4 produced a very low onset potential of −500 mV, corresponding to a very low current density of −2.7 mA/cm^2 for the HER. This catalyst is poor toward the HER. However, the pairing of CQDs with g-C_3N_4 is somewhat better because of the strong (spontaneous sp^2 and sp^3 hybridization) electrostatic interactions between them [71, 72]. Clusters of Ti^{3+}/Ti^{4+} ions and intraplanar and interplanar stacking structures of g-C_3N_4 are considered to cause H-O-H cleavage and provide active sites for the adsorption of hydrogen species [73]. The electrons of the delocalized π−conjugated network of CQDs effectively participate in the reduction process, leading to hydrogen production [74]. The sample with 15.0 mL of CQDs had a small onset potential (−370 mV) and greater current density (−33 mA/cm^{2}2) than the other samples did. Catalysts with 10.0 mL and 20.0 mL of CQDs generate onset potentials of −440 mV and −406 mV related to current densities of −4.8 and 17.0 mA/cm^2, respectively. A decrease in HER activity was noted above 15.0 mL of CQDs. The catalyst can become saturated with a high amount of foreign material, and the active centers of the catalyst deteriorate, which reduces its efficiency. Figure 10 (B) shows the Nyquist plots of the samples. A very high charge transfer resistance (Rct) was noted for TiO_2/g-C_3N_4 and TiO_2/g-C_3N_4 (20.0 mL). The samples with 10.0 and 15.0 mL of CQDs produced Rct values of −831 Ω and −1032 Ω, respectively. A small value of Rct is beneficial for conduction and reduction processes during photoelectrocatalysis. Figure 11 depicts a systematic approach for photoelectrochemical (PEC) water splitting on a TiO_2/g-C_3N_4 photoelectrode.

To assess the charge, transfer properties of the produced photocatalysts, electrochemical impedance spectroscopy (EIS) was used. According to the Nyquist plots (Fig. 10 (B)), the Rct value of the 15.0 mL CQDs/TiO_2/g-C_3N_4 composite was approximately 1032 Ω, which was much lower than that of the TiO_2/g-C_3N_4 (∼ 2700 Ω) and the 20.0 mL CQD-loaded sample (∼ 2400 Ω). An intermediate Rct of around 831 Ω was observed in the 10.0 mL CQD-loaded sample as shown in Table 4.

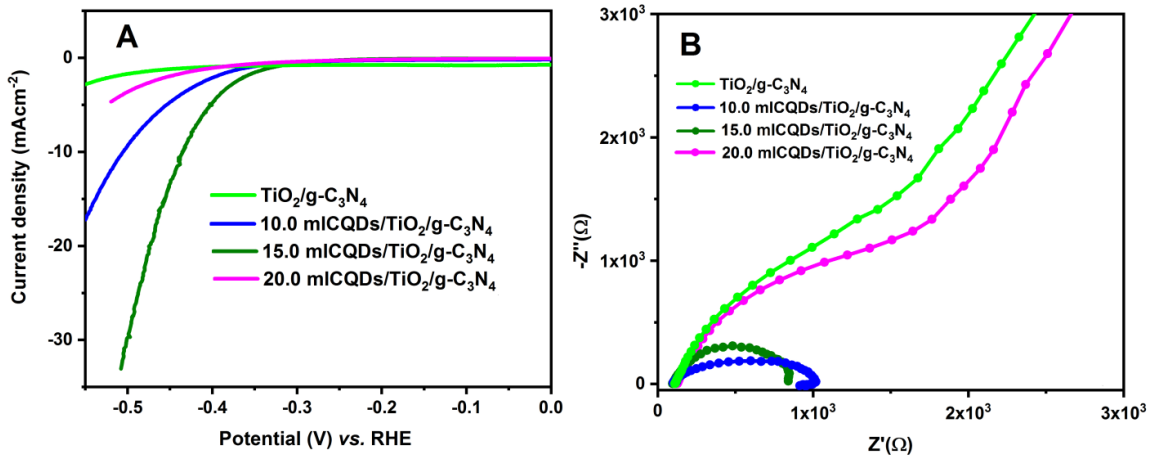

Figure 10. (A) Polarization curves of TiO_2/g-C_3N_4 and CQDs/TiO_2-g-C_3N_4 with concentrations of 10.0, 15.0 and 20.0 mL of CQDs obtained via LSV for the HER (0.5 M KOH) at a scan rate of 5 mV/s. (B) Corresponding Nyquist plots of the samples.

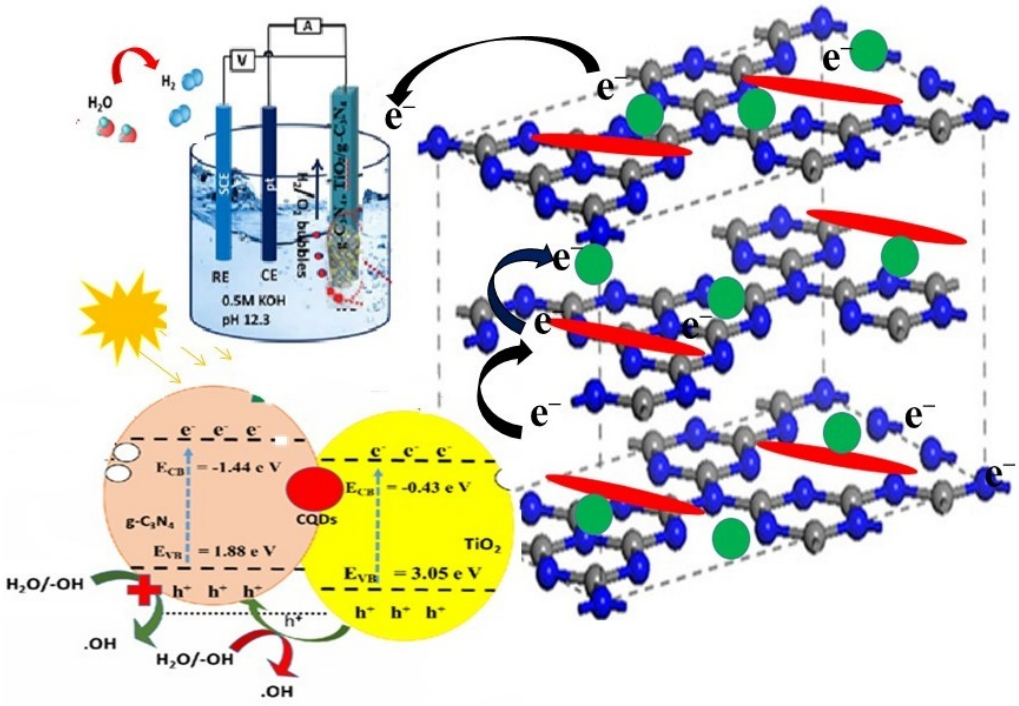

Figure 11. Systematic approach for photoelectrochemical water splitting on 2D g-C_3N_4 modified with 1D TiO_2 and CQD (CQD/TiO_2/g-C_3N_4) photoelectrodes.

Table 4. Quantitative comparison between the corresponding photocurrent densities derived from PEC measurements and Rct (Ω) values:

Sample	Rct (Ω)	Photocurrent Density (mA/cm^2)
TiO_2/g-C_3N_4	∼ 2700 Ω	2.7
10.0 mL CQDs/TiO_2/g-C_3N_4	∼ 831 Ω	4.8
15.0 mL CQDs/TiO_2/g-C_3N_4	∼ 1032 Ω	33.0
20.0 mL CQDs/TiO_2/g-C_3N_4	∼ 2400 Ω	17.0

9. Conclusions

In summary, CQD/TiO_2/g-C_3N_4 ternary nanocomposites were successfully synthesized to exploit multidimensional (0D/1D/2D) haterostructures for enhanced photocatalytic and photoelectrochemical (PEC) performance under visible light. The incorporation of CQDs significiently improved visible absorption, suppressed electron-hole recombination, and facilitated charge transfer, as confirmed by photoluminescences (PL) quenching and UV-Visi DRS analysis. The 15.0 and 20.0 mL of the CQD/TiO_2/g-C_3N_4 composite achieved superior degradation efficiency of methyl orange (MO) and bromophenolblue (BPB) under visible light irradiation ($\lambda > 420$), reaching up to 96.0 and 82.0% outperforming g-C_3N_4 and binary composites. The MO & BPB are degraded in various sources of water, drain water, stream water, rainwater, and tap water as well. The PEC measurements showed a marked enhancement in photocurrent density, the optimized CQDs/TiO_2-g-C_3N_4 (15.0 mL) ($j^{1/4} \sim 33$ mA/cm^2) exhibited a stable photo-electrocatalytic response throughout the PEC process due to improved charge separation and quick hole extraction. Moreover, effective CQD deposition onto the TiO_2/g-C_3N_4 hetrostructure significantly improved the PEC performance, even at higher energy potentials and improved the chemical stability of TiO_2-incorporated photocatalysts. The synergistic interactions between the CQDs and TiO_2/g-C_3N_4 haterostructure played avital role in the boosting overall photocatalytic activity. This work takes advantage of electron mediator/transfer property of CQDs between the interface of the CQDs and TiO_2/g-C_3N_4 to improve the charge separation efficiency. The study demonstrates that the rational design of multidimensional haterojunctions (TiO_2/g-C_3N_4) with conductive CQDs to increase stability and visible light response can be used to create new CQD combinations that are connected with g-C_3N_4 frameworks. The 15.0 mL loading was found optimal as it ensured sufficient surface coverage and efficient charge transfer whereas excessive loading (20.0 mL) led to aggregation, limiting active sites. Moreover, this study acknowledges that further evaluation with real industrial wastewater is required to validate large-scale application. Future work will explore the optimization of CQDs loading, long term stability under solar conditions and application to real wastewater treatment and hydrogen generation system. Although the fabricated CQD/TiO_2/g-C_3N_4 composites'

photocatalytic performance was shown using prototypical organic dyes in an organized laboratory venue, further research applying real industrial wastewater models is crucial to entirely evaluate the developed photocatalysts' large-scale potential and actual applicability. This study is a component for practical potential on future research in evaluating considerable wastewater scenarios.

Acknowledgment
This work has been acknowledged to International Islamic University Islamabad and Pakistan Institute of Engineering and Applied Sciences (PIEAS) Islamabad Pakistan.

Authors Contribution
Authors have contributed equally in preparing and writing the manuscript.

Availability of data and materials
The datasets generated and/or analyzed during the current study are available from the corresponding author on reasonable request. All data supporting the findings of this study are included within the article and its supplementary materials, where applicable.

Conflict of interests
The authors declare that they have no known competing financial interests or personal relationships that could have appeared to influence the work reported in this paper.

References

[1] H. Jabeen, R.S. Haider, S. Sajjad, S.A.K. Leghari, N. Noor, M.A. Amin, and Ibrahim. M.M. "Advances in modifications of Ag/g-C_3N_4 for stable and effective photoanode for OER". *Opt Mater*, **145**: 114376, 2023.

[2] Q. Gao, M. Wang, Y. Zhu, Y. Chai, and B. Liu. "Facile Construction of CdS/g-C_3N_4 Photocatalyst for Enhanced Removal of Methyl Orange ". Water, Air, & Soil Pollution(7):427, 2025.

[3] S.A.K. Leghari, S. Sajjad, and J. Zhang. "A time saving and cost effective route for metal oxides activation.". *RSC Adv*, **4**:5248–5253, 2014.

[4] Z. Yousaf, S. Sajjad, S.A.K. Leghari, and Z. ElBahy. "Influence of integrated nitrogen functionalities in nitrogen doped graphene modified WO_3 functional visible photocatalyst". J Environ Chem Eng:106746, 2021.

[5] R.T. Guo, J. Wang, Z.-X. Bi, X. Chen, X. Hu, and W.G. Pan. "Recent advances and perspectives of g–C_3N_4–based materials for photocatalytic dyes degradation". *Chemosphere*, **287**:132132, 2022.

[6] C. Thambiliyagodage, A. Kumara, M. Jayanetti, L. Usgodaarachchi, H. Liyanaarachchi, and B. Lansakara. "Fabrication of dual Z-scheme g-C_3N_4/Fe_2TiO_5/Fe_2O_3 ternary nanocomposite using natural ilmenite for efficient photocatalysis and photosterilization under visible light". *Appl Surf Sci Adv*, **12**:100337, 2022.

[7] M.A. Qamar, M. Javed, S. Shahid, M. Shariq, M.M. Fadhali, S.K. Ali, and M.S. Khan. "Synthesis and applications of graphitic carbon nitride (g-C_3N_4) based membranes: A review". *Heliyon*, **9**:12685, 2023.

[8] J. Pan, M. You, C. Chi, Z. Dong, B. Wang, M. Zhu, and C. Li. "The two dimension carbon quantum dots modified porous g-C_3N_4/TiO_2 nano-heterojunctions for visible light hydrogen production enhancement". *Int J Hydrogen Energy*, (13):6586–6593, 2018.

[9] S. Panimalar, R. Uthrakumar, E.T. Selvi, P. Gomathy, C. Inmozhi, K. Kaviyarasu, and J. Kennedy. "Studies of MnO_2/g-C_3N_4 heterostructure efficient of visible light photocatalyst for pollutants degradation by sol-gel technique". *Int J Hydrogen Energy*, **45**: 11501–11510, 2020.

[10] M. Nemiwal, T.C. Zhang, and D. Kumar. "Recent progress in g-C_3N_4, TiO_2 and ZnO based photocatalysts for dye degradation: Strategies to improve photocatalytic activity". *Sci Total Environ*, **767**:144896, 2021.

[11] H. Liyanaarachchi, C. Thambiliyagodage, C. Liyanaarachchi, and U. Samarakoon. "Efficient photocatalysis of Cu doped TiO_2/g-C_3N_4 for the photodegradation of methylene blue". *Arabian J Chem*, **16**: 104749, 2023.

[12] M. Zhu, C. Zhai, M. Sun, Y. Hu, B. Yan, and Y. Du. "Ultrathin graphitic C_3N_4 nanosheet as a promising visible-light-activated support for boosting photoelectrocatalytic methanol oxidation". *Appl Catal B Environ*, **203**:108–115, 2017.

[13] L. Kong, J. Wang, X. Mu, R. Li, X. Li, X. Fan, and M. Sun. "Porous size dependent g-C_3N_4 for efficient photocatalysts: regulation syntheses and physical mechanism". *Mater Today Energy*, **13**:11–21, 2019.

[14] L. Wang, K. Wang, T. He, Y. Zhao, H. Song, and H. Wang. "Graphitic carbon nitride-based photocatalytic materials: Preparation strategy and application". *ACS Sustainable Chemistry & Engineering*, **8**(43): 16048–16085, 2020.

[15] S. Karimkhani, P. Derakhshi, P. Aberoomand Azar, and S.M. Sheikh-Al-Eslamian. "Facile, fast, and green preparation of high-purity and quality silica nanoparticles using a handmade ball mill: Comparison with the sol–gel method". *J Nanostruct Chem*, **14**:369–381, 2016.

[16] S. Abbas, B. Uzair, S. Sajjad, S.A.K. Leghari, S. Noor, M.B. Khan Niazi, I. Farooq, and H. Iqbal. "Dual-Functional Green Facile CuO/MgO Nanosheets Composite as an Efficient Antimicrobial Agent and Photocatalyst". *Arab J Sci Eng*, **47**:5895–5909, 2022.

[17] S. Noor, S. Sajjad, S.A.K. Leghari, C. Flox, and S. Ahmad. "Competitive role of nitrogen functionalities of N doped GO and sensitizing effect of Bi_2O_3 QDs on TiO_2 for water remediation". *J Environ Sci*, **108**:107–119, 2021.

[18] G.S. Jamila, S. Sajjad, S.A.K. Leghari, M. Mehboob, and C. Flox. "Enhanced electron transport by Fe_2O_3 on NCQDs–MgO nanostructure for solar photocatalysis and electrocatalytic water splitting". *Appl Nanoscience*, **12**:1815–1827, 2022.

[19] Z. Xu, Y. Wang, J. Zhuang, Y. Li, and L. Jia. "High temperature hydrothermal etching of g-C_3N_4 for synthesis of N-doped carbon quantum dots-supported CdS photocatalyst to enhance visible light driven hydrogen generation". *Molecular Catalysis*, **517**:111900, 2022.

[20] Z. Yousaf, S. Sajjad, S.A.K. Leghari, M. Mehboob, A. Kanwal, and B. Uzair. "Interfacial charge transfer via 2D-NiO and 2D-graphene nanosheets combination for significant visible photocatalysis". *J Solid State Chem*, **287**:121606, 2020.

[21] Y.J. Zou, J.W. Shi, D.K. Ma, Z.P. Fan, and C.G. Niu. "In situ synthesis of C-doped TiO_2@g-C_3N_4 core–shell hollow nanospheres with enhanced visible-light photocatalytic activity for H_2 evolution". *Chem Eng J*, **322**:435–444, 2017.

[22] H.M. Solayman, A. Abd Aziz, N.Y. Yahya, K.H. Leong, L.C. Sim, M.K. Hossain, and K.D. Zoh. "CQDs embed g-C_3N_4 photocatalyst in dye removal and hydrogen evolution An insight review". *J Water Process Eng*, **57**:104645, 2024.

[23] J. Pan, M. You, C. Chi, Z. Dong, B. Wang, M. Zhu, and C. Li. "The two-dimension carbon quantum dots modified porous g-C_3N_4/TiO_2 nano heterojunctions for visible light hydrogen production enhancement". *Int J Hydrogen Energy*, **43**:6586–6593, 2018.

[24] H. Jindal, D. Kumar, M. Sillanpaa, and M. Nemiwal. "Current progress in polymeric graphitic carbon nitride-based photocatalysts for dye degradation". *Inorg Chem Commun*, **129**:108786, 2021.

[25] X. Liu, Z. Yang, Y. Yang, and H. Li. "Construction of carbon quantum dots sensitized porous carbon nitride/titanium dioxide nanosheets for enhancing visible light photocatalytic degradation of tetracycline". *Chem Eng J*, **446**:108083, 2022.

[26] U. Abd Rani, L.Y. Ng, C.Y. Ng, and E. Mahmoudi. "A review of carbon quantum dots and their applications in wastewater treatment". *Adv Colloid Interface Sci*, **278**:102124, 2020.

[27] Y. Wang, X. Wang, and M. Antonietti. "Polymeric graphitic carbon nitride as a heterogeneous organocatalyst: From photochemistry to multipurpose catalysis to sustainable chemistry". Angew Chem Int Ed:68–89, 2012.

[28] Y. Zhang, T. Mori, J. Ye, and M. Antonietti. "Phosphorus-doped carbon nitride solid: Enhanced electrical conductivity and photocurrent generation". J Am Chem Soc:6294–6295, 2010.

[29] S. Cao, J. Low, J. Yu, and M. Jaroniec. "Polymeric photocatalysts based on graphitic carbon nitride". *Adv Mater*, **27**(13):2150–2176, 2015.

[30] S. Shamaila, A.K.L. Sajjad, F. Chen, and J. Zhang. "Synthesis and characterization of mesoporous TiO_2 with enhanced photocatalytic activity for the degradation of chlorophenol". *Mater Res Bull*, **45** (45):1375–1382, 2010.

[31] X. Liu, Y. Yang, H. Li, Z. Yang, and Y. Fang. "Visible light degradation of tetracycline using oxygen-rich titanium dioxide nanosheets decorated by carbon quantum dots". *Chem Eng J*, **408**:127259, 2021.

[32] W.J. Ong, L.L. Tan, S.P. Chai, and S.T. Yong. "Heterojunction engineering of graphitic carbon nitride (g-C_3N_4) via Pt loading with improved daylight-induced photocatalytic reduction of carbon dioxide to methane". *Dalton Trans*, **44**(3):1249–1257, 2015.

[33] J. Jiang, L. Ou-yang, L. Zhu, A. Zheng, J. Zou, X. Yi, and H. Tang. "Dependence of electronic structure of g-C_3N_4 on the layer number of its nanosheets: A study by Raman spectroscopy coupled with first-principles calculations". *Carbon*, **80**:213–221, 2014.

[34] S. Kumar, D. Nayak, S. Ansari, J. Bauri, and R.B. Choudhary. "Investigation of structural, optical and thermal properties of TiO_2 reinforced g-C_3N_4 nanocomposite for emissive layer application". *Mater Today Proc*, **84**:557–562, 2023.

[35] A.B. Naveed, A. Javaid, A. Zia, M.T. Ishaq, M. Amin, Z.U.R. Farooqi, and A. Mahmood. "TiO_2/g-C_3N_4 binary composite as an efficient photocatalyst for biodiesel production from Jatropha oil and dye degradation". *ACS Omega*, **8**(2):2173–2182, 2023.

[36] G. Sarp, E. Yildirim, and E. Akyol. "g-C_3N_4@TiO_2@Fe_3O_4 multifunctional nanomaterial for magnetic solid-phase extraction and photocatalytic degradation-based removal of trimethoprim and isoniazid". *ACS Omega*, **7**(27):23223–23233, 2022.

[37] J. Wang, J. Huang, H. Xie, and A. Qu. "Synthesis of g-C_3N_4/TiO_2 with enhanced photocatalytic activity for H_2 evolution by a simple method". *Int J Hydrogen Energy*, **39**:6354–6363, 2014.

[38] R. Fagan, D.E. McCormack, S.J. Hinder, and S.C. Pillai. "Photocatalytic properties of g-C_3N_4–TiO_2 heterojunctions under UV and visible light conditions". *Materials*, **9**(4):286, 2016.

[39] X. Liu, Y. Yang, H. Li, Z. Yang, and Y. Fang. "Visible light degradation of tetracycline using oxygen-rich titanium dioxide nanosheets decorated by carbon quantum dots". *Chem Eng J*, **408**:127259, 2021.

[40] Y. Deng, M. Chen, G. Chen, W. Zou, Y. Zhao, H. Zhang, and Q. Zhao. "Visible–Ultraviolet Upconversion Carbon Quantum Dots for Enhancement of the Photocatalytic Activity of Titanium Dioxide". *ACS Omega*, **6**(6):4247–4254, 2021.

[41] Y. Su, P. Chen, F. Wang, Q. Zhang, T. Chen, Y. Wang, and G. Liu. "Decoration of TiO_2/g-C_3N_4 Z-scheme by carbon dots as a novel photocatalyst with improved visible-light photocatalytic performance for the degradation of enrofloxacin". *RSC Adv*, **7**(54):34096–34103, 2017.

[42] W. Liu, Y. Li, F. Liu, W. Jiang, D. Zhang, and J. Liang. "Visible-light-driven photocatalytic degradation of diclofenac by carbon quantum dots modified porous g-C_3N_4: Mechanisms, degradation pathway and DFT calculation". *Water Res*, **151**:8–19, 2019.

[43] K. Hu, M. Yao, Z. Yang, G. Xiao, L. Zhu, H. Zhang, and B. Liu. "Pressure tuned photoluminescence and band gap in two-dimensional layered g-C_3N_4: The effect of interlayer interactions". *Nanoscale*, **12**(23):12300–12307, 2020.

[44] S. Noor, R.S. Haider, S. Noor, S. Sajjad, S.A.K. Leghari, M. Mehboob, and M. Long. "Role of conductive channels via CQDs on NiO/g-C_3N_4 Z-scheme composite as a bifunctional photocatalyst". *Int J Hydrogen Energy*, **47**(86):36517–36529, 2022.

[45] G. Li, J. Huang, N. Wang, J. Huang, Y. Zheng, G. Zhan, and Q. Li. "Carbon quantum dots functionalized g-C_3N_4 nanosheets as enhanced visible-light photocatalysts for water splitting". *Diam Relat Mater*, **116**:108242, 2021.

[46] B. Ren, T. Wang, G. Qu, F. Deng, D. Liang, W. Yang, and M. Liu. "In situ synthesis of g-C_3N_4/TiO_2 heterojunction nanocomposites as a highly active photocatalyst for the degradation of Orange II under visible light irradiation". *Environ Sci Pollut Res*, **25**(19): 19122–19133, 2018.

[47] W. Wang, J. Fang, S. Shao, M. Lai, and C. Lu. "Compact and uniform TiO_2@g-C_3N_4 core-shell quantum heterojunction for photocatalytic degradation of tetracycline antibiotics". *Appl Catal B Environ*, **217**: 57–64, 2017.

[48] F. O. Alqahtani. "Advancing photocatalytic degradation under visible light with TiO_2/g-C_3N_4 nanohybrid mechanistic insights". *Journal of Saudi Chemical Society*, **28**(5):1234–1245, 2024.

[49] D.T.N. Hoa, N.T.T. Tu, H.Q.A. Thinh, L. Van Thanh Son, L.V.T. Son, N.D.V. Quyen, and D.Q. Khieu. "TiO_2/g-C_3N_4 Visible-Light-Driven Photocatalyst for Methylene Blue Decomposition.". *Journal of Nanomaterials*, **2023**(1):9967890, 2023.

[50] W. Liu, Y. Li, F. Liu, D. Jiang, W.a nd Zhang, and J. Liang. "Visible-light-driven photocatalytic degradation of diclofenac by carbon quantum dots modified porous g-C_3N_4: Mechanisms, degradation pathway and DFT calculation". *Water Res*, **151**:8–19, 2019.

[51] T. Jin, C. Liu, F. Chen, J. Qian, Y. Qiu, X. Meng, and Z. Chen. "Synthesis of g-C_3N_4/CQDs composite and its photocatalytic degradation property for Rhodamine B". *Carbon Lett*, **32**:1451–1462, 2022.

[52] D. Vidyasagar, S.G. Ghugal, A. Kulkarni, P. Mishra, and A.G. Shende. "Silver/Silver(II) oxide (Ag/AgO) loaded graphitic carbon nitride microspheres: an effective visible light active photocatalyst for degradation of acidic dyes and bacterial inactivation". *Appl Catal B Environ*, **221**(10).

[53] R. Mohini and N. Lakshminarasimhan. "Coupled semiconductor nanocomposite g-C_3N_4/TiO_2 with enhanced visible light photocatalytic activity". *Mater Res Bull*, **76**:370–375, 2016.

[54] Z. Lu, L. Zeng, W. Song, Z. Qin, D. Zeng, and C. Xie. "In situ synthesis of C-TiO_2/g-C_3N_4 heterojunction nanocomposite as highly visible light active photocatalyst originated from effective interfacial charge transfer". *Appl Catal B Environ*, **202**:489–499, 2017.

[55] J.J. Zhang, S.S. Fang, J.Y. Mei, G.P. Zheng, X.C. Zheng, and X.X. Guan. "High efficiency removal of rhodamine B dye in water using g-C_3N_4 and TiO_2 cohybridized 3D graphene aerogel composites". *Sep Purif Technol*, **194**:96–103, 2018.

[56] S. Das and H. Mahalingam. "Dye degradation studies using immobilized pristine and waste polystyrene-TiO_2/rGO/g-C_3N_4 nanocomposite photocatalytic film in a novel airlift reactor under visible light irradiation". *Sci. Total Environ*, **690**:370–384, 2019.

[57] S. Feng, T. Chen, Z. Liu, J. Shi, X. Yue, and Y. Li. "Z-scheme CdS/CQDs/g-C_3N_4 composites with visible-near-infrared light response for efficient photocatalytic organic pollutant degradation". *Sci Total Environ*, **704**:135404, 2020.

[58] L. Hu, J. Yan, C. Wang, B. Chai, and J. Li. "Direct electrospinning method for the construction of Z-scheme TiO_2/g-C_3N_4/RGO ternary heterojunction photocatalysts with remarkably ameliorated photocatalytic performance". *Chin J Catal*, **40**(3):458–469, 2019.

[59] R. Liu, Y. Bie, Y. Qiao, T. Liu, and Y. Song. "Design of g-C_3N_4/TiO_2 nanotubes heterojunction for enhanced organic pollutants degradation in wastewater". *Mater Lett*, **251**:126–130, 2019.

[60] H. Ji, P. Du, D. Zhao, S. Li, F. Sun, E. C. Duin, and W. Liu. "2D/1D graphitic carbon nitride/titanate nanotubes heterostructure for efficient photocatalysis of sulfamethazine under solar light: Catalytic "hot spots" at the rutile–anatase–titanate interfaces ". Appl Catal B Environ:118357, 2020.

[61] P. Gündoğmuş, J. Park, and A. Öztürk. "Preparation and photocatalytic activity of g-C_3N_4/TiO_2 heterojunctions under solar light illumination". *Ceram Int*, **46**(13):21431–21438, 2020.

[62] A. Khan, R. Jonathan, S.U. Rehman, M. Shoaib, F. Cao, S. Ali, and X. Jian. "Ultra-fine carbon decorated TiO_2/C/g-C_3N_4 hybrid for strong physical adsorption and efficient photodegradation of pollutants.". Arab J Chem(1):106034, 2025.

[63] M. Tian, C. Hu, J. Yu, and L. Chen. "Carbon quantum dots (CQDs) mediated Z-scheme g-C_3N_4–CQDs/$BiVO_4$ heterojunction with enhanced visible light photocatalytic degradation of Paraben". *Chemosphere*, **308**:138248, 2023.

[64] Y. Xu, W. Hou, K. Huang, H. Guo, Z. Wang, C. Lian, and L. Wang. "Engineering built-in electric field microenvironment of CQDs/g-C_3N_4 heterojunction for efficient photocatalytic CO_2 reduction". *Adv Sci (Weinh.)*, **11**(28):2403607, 2024.

[65] M. Shoaib, M.Y. Naz, S. Shukrullah, M.A. Munir, M. Irfan, S. Rahman, and A.A.J. Ghanim. "Dual S-scheme heterojunction CdS/TiO_2/g-C_3N_4 photocatalyst for hydrogen production and dye degradation applications". *ACS Omega*, **8**(45):43139–43150, 2023.

[66] F. Iram, A.M. Mallah, M. Safdar, M. Khitouni, B. Hammami, H.A.H. Alsehaibani, and I.S. Alkhaibari. "Fabrication and OER/HER electrochemical activity of Sm, Al assisted g-C_3N_4 nanocomposite for alkaline water splitting". *Journal of Alloys and Compounds*, **1014**: 178603, 2025.

[67] L. Zhang, X. Yang, Z. Yin, and L. Sun. "A review on carbon quantum dots: Synthesis, photoluminescence mechanisms and applications". *Luminescence*, **37**(10):1612–1638, 2022.

[68] H. Noreen, A. Farooq, S. Naz, N. Amjed, A. Ahmad, A. Aftab, and S. Muzammal. "From lab to environment: A critical eye approach toward morphological synthesis of graphitic carbon nitride for environmental restoration". *Journal of the Iranian Chemical Society*, pages 1–24, 2025.

[69] C. Liu, J. Wang, H. Xu, Y. Li, and H. Zhang. "Photo-Fenton degradation of tetracycline over Z-scheme Fe-g-C_3N_4/Bi_2WO_6 heterojunctions: Mechanism insight, degradation pathways and DFT calculation". *Appl Catal B Environ*, **310**:121326–121340, 2022.

[70] A. Pandey, U. Alam, A. Gupta, J.J. Shim, and N. Verma. "S-scheme heterojunction-mediated hydrogen production over the graphitic carbon nitride-anchored nickel stannate perovskite". *Fuel*, **355**:129538, 2024.

[71] K. Ashok, P. Rosaiah, D. Radhalayam, F.A.M. Al-Zahrani, and M. Suneetha. "Enhancing photocatalytic efficiency and hydrogen production through oxygen-defective g-C_3N_4/Fe_2O_3 composites". *Diamond and Related Materials*, page 112851, 2025.

[72] A.S.S. Bilal, U. Bilal, T. Abbas, R. Roopashree, E. Khudoynazarov, M. Yaxshimuratov, and H.M. Noman. "Enhanced solar-driven hydrogen evolution via C_3N_4/NiO/ZnO ternary heterojunction nanocomposite with efficient charge separation". Next Energy:100417, 2025.

[73] F. Iram, A.M. Mallah, M. Safdar, M. Khitouni, B. Hammami, H.A.H. Alsehaibani, and I.S. Alkhaibari. "Fabrication and OER/HER electrochemical activity of Sm, Al assisted g-C_3N_4 nanocomposite for alkaline water splitting". *Journal of Alloys and Compounds*, **1014**: 178603, 2025.

[74] C.W. Backes, F.B. Reis, G.B. Strapasson, M. Assis, E. Longo, and D.E. Weibel. "Green Synthesis of carbon quantum dots for enhancing photocatalytic activity: Hydrogen/oxygen evolution and dye photodegradation". Catalysis Today:114996, 2025.